Made available for a limited time for personal research and study only License.

ACS APPLIED OPTICAL MATERIALS

pubs.acs.org/acsaom Article

Circularly Polarized Photoluminescence from Nanostructured Arrays of Light Emitters

Maya Ramamurthy, Pavlos Pachidis, Bryan M. Cote, and Vivian E. Ferry*

Cite This: ACS Appl. Opt. Mater. 2023, 1, 491−499 Read Online

ACCESS | Metrics & More | Article Recommendations | Supporting Information

ABSTRACT: Strategically designed metamaterials can influence the properties of light emitters in several ways, including shaping of the directionality and polarization of luminescence. These properties, however, are limited in systems where the luminophores uniformly coat the metamaterial. Here, we study and design metamaterials composed of both Au nanobars and nanopatterned light emitters. We systematically investigate the role of spatial averaging, dipole orientation, chirality, near-field effects, and other factors for these multimaterial systems. Finally, we discuss multiple design routes to create metasurfaces that can emit photoluminescence of any circular polarization at any arbitrary angle. These systems simultaneously exhibit high photoluminescence intensity and tailored, directional, and polarized photoluminescence.

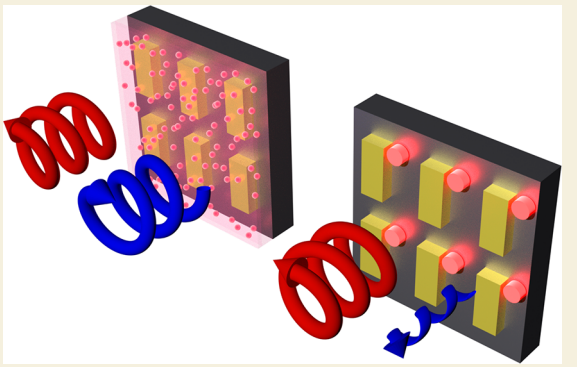

KEYWORDS: *metasurface, chirality, k-space polarimetry, quantum dot, polarized luminescence, lattice resonance*

Downloaded via UNIV OF MINNESOTA on February 20, 2023 at 20:12:43 (UTC).
See https://pubs.acs.org/sharingguidelines for options on how to legitimately share published articles.

INTRODUCTION

Periodic nanostructure arrays allow for exceptional control of light−matter interactions at the nanoscale, manipulating the phase,[1−3] polarization,[4−7] and directionality of incident electromagnetic radiation.[8−12] The development of metasurfaces in particular has opened up new, compact routes to spatial and spectral shaping of luminescence via coupling to nearby luminophores.[13−15] Among the many possibilities, new routes to realize circularly polarized luminescence are especially attractive for a number of emerging applications, including security tags, stereoscopic displays, and unidirectional light propagation in photonic circuits.[16−18] By coupling photoluminescent (PL) materials to achiral or chiral nanostructures, systems have been developed that exhibit right or left circularly polarized PL (RCP/LCP) along specific angles in the far-field.[19−22]

In most of the work shown to date, light emitters uniformly coat the metasurface.[23,24] However, more complex and controlled effects could be realized by placing the emitters in specific locations, as has been studied for linear polarization,[25] or by creating metasurface components directly from light-emitting materials.[22,26] We are particularly interested in systems with *patterned* light emitters that form hierarchical nanostructures with their own collective properties, a case that is distinctly different from either uniform films or individual emitters. We and others have recently shown that such structures can be realized using direct-write electron beam lithographic patterning of semiconductor nanocrystals.[27−31] In this paper, we show that the deliberate placement of a luminescent pattern in the unit cell of a metasurface creates systems with significantly higher degrees of circular polarization (DCP) than systems where the metasurface is covered uniformly by a luminescent film and that, crucially, this control over polarization is realized at the same angles where the PL intensity is high.

RESULTS AND DISCUSSION

For our numerical simulations, we use a periodic array of gold nanorods, as shown in Figure 1a. The gold nanorods have lateral dimensions of 160 nm × 300 nm, are 70 nm thick, and are arranged in a square periodic lattice with pitch p = 600 nm. We chose this single nanorod case because it is a simple initial case to analyze. Although this system is achiral at normal incidence, it is chiral under oblique incidence.[32] Light propagation in this system is highly dependent on the refractive index of each component.[33] The refractive index also dictates how and where electromagnetic fields are concentrated. The system rests on a 130 nm thick layer of refractive index n = 1.8, chosen to approximate a layer of indium tin oxide (ITO), placed on top of an n = 1.52 glass substrate. Glass/ITO substrates were chosen because they are electrically conductive and optically transparent, enabling the

Received: October 17, 2022
Accepted: December 15, 2022
Published: January 5, 2023

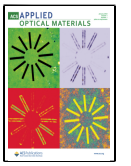

ACS Publications © 2023 American Chemical Society

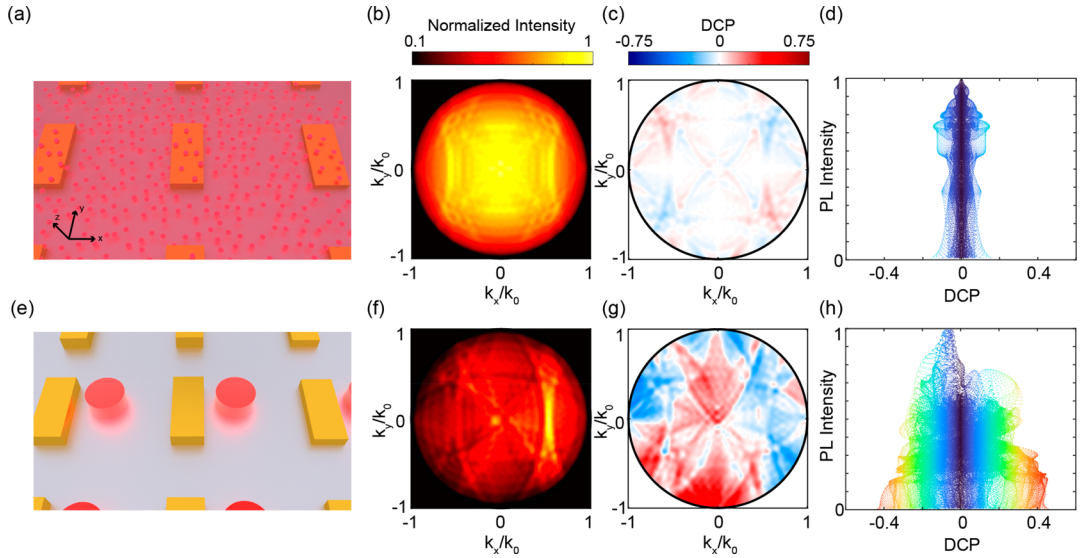

Figure 1. (a) Schematic of gold nanobars covered in a film of light emitters, (b) the corresponding normalized Fourier-space photoluminescence intensity, and (c) DCP of the luminescent film. (d) DCP vs PL intensity for the film. Color represents the magnitude of the DCP. (e) Schematic of a nanostructured solid of light emitters near the gold nanobars, (f) the corresponding normalized Fourier-space photoluminescence intensity, and (g) DCP of the array with the nanostructured solid. (h) DCP vs PL intensity for the nanostructured solid of light emitters. Color represents the magnitude of DCP.

structures to be fabricated by electron-beam lithography methods and allowing for characterization of the transmitted PL. Figure 1a–d considers the case where the array of Au nanorods is covered in an 88 nm thick luminescent film with constant refractive index n = 1.59, taken from previous measurements of the refractive index of poly(lauryl methacrylate) (PLMA)–CdSe/CdS composite films. The dipoles emit at λ_{PL} = 630 nm.

We use finite difference time domain (FDTD) simulations to calculate the angular projection and polarization state of the PL in the far-field, similarly to measurements performed using Fourier-space polarimetry.[34−37] The luminescent film was simulated by embedding dipole emitters at various locations within a dielectric film. A single simulation captures one particular dipole orientation, but the simulations are repeated for the two other orthogonal dipole orientations and averaged to capture the random nature of the dipole's orientation. Further details of the simulation procedure are described in the Method of Calculation section, and the effects of dipole orientation are discussed in more detail later in the paper. To quantify DCP, we use the

$$\mathrm{DCP} = \frac{S_3}{S_0} = \frac{I_{\mathrm{RCP}} - I_{\mathrm{LCP}}}{I_{\mathrm{RCP}} + I_{\mathrm{LCP}}}$$

which is based on the first and fourth Stokes parameters. The sign of S_3 denotes the handedness of circular polarization: positive S_3 signifies higher intensity of RCP light while negative S_3 signifies higher intensity of LCP light.

Figure 1b shows the calculated PL intensity from the film. The data shows clear branches at specific vectors in Fourier space, which follow the Rayleigh–Wood (RW) expressions for oblique incidence,[38] where the effective mode index is determined by the modes supported by the system and substrate.[26,39,40] These follow the equation

$$\left(\frac{2\pi}{\lambda_{\mathrm{PL}}}n\right)^2 = \left(k_{\mathrm{out},x_{\parallel}} - i\frac{2\pi}{\mathrm{pitch}}\right)^2 + \left(k_{\mathrm{out},y_{\parallel}} - j\frac{2\pi}{\mathrm{pitch}}\right)^2$$

where λ_{PL} is the center wavelength of the PL, i and j denote the different RW modes, and n is the refractive index of the guided mode that is injected into or emitted from the system. In a 3D nanostructure made up of multiple materials with different refractive indices, the relevant n is the effective refractive index (n_{eff}), where n_{eff} is the result of collapsing a 3D geometry into a 2D set of effective indices. The effective index that was chosen for the calculation of the RW lines is the one that gives the highest electric field overlap with the emitters in the system. For this case of dipoles in a film of PLMA, the mode with the highest electric field overlap with the emitters has an index of n_{eff} = 1.59. The RW modes visible in this system correspond to the (0, ±1), (±1, 0), (±1, ±1), and (±2, 0) modes at n_{eff} = 1.59 and are shown overlaid on Figure 1b,c in Figure S1a,c.

The DCP k-space data of the system with the uniform film shows very small areas with significant magnitude. Comparing the normalized PL intensity to the DCP k-space data of the system, we observe that these small areas with significant magnitude of DCP are concentrated at angles where the PL intensity is small. To better visualize the connection between the PL intensity and the DCP, Figure 1d merges the data in Figure 1b,c: for each point, the DCP and the PL intensity are plotted against one another. The color scale is a guide for the eye and represents the magnitude of the DCP. This clearly indicates that the DCP is low throughout the k-space distribution.

In contrast, ensembles of light emitters strategically placed at specific areas in the unit cell of the plasmonic array exhibit a substantially higher magnitude of DCP in the far-field. Figure 1e shows a system consisting of 88 nm tall nanopillars of light emitters with a diameter of 140 nm. As mentioned earlier, these structures can be fabricated by direct-write electron-beam lithography methods, which allow for the placement and patterning of an ensemble of quantum dot (QD) nanocrystals.[27−31] The refractive index of the pillar was set to n = 1.75 to match previously measured data for nanocrystal solids.[33] The 88 nm tall pillar was modeled by placing dipoles at four different heights inside the structure (z = 20 nm, z = 40 nm, z

https://doi.org/10.1021/acsaom.2c00130
ACS Appl. Opt. Mater. 2023, 1, 491−499

= 60 nm, and z = 80 nm), and averaging the results given by each position. The k-space PL intensity data in Figure 1f shows RW modes with n_{eff} = 1.55 (shown in Figure S1b,d), but the intensity is no longer symmetric with respect to angle. Figure 1g shows that the DCP k-space data exhibits substantial DCP along most k-vectors, unlike in the case of the uniform film of emitters. Figure 1h shows that even though the highest DCP regions exhibit low PL, there are regions where the DCP and PL intensity are simultaneously moderately high (|DCP| > 0.2 and I > 0.5). Such regions do not exist for the case of the uniform film of emitters.

One reason for the improved PL intensity/DCP of the patterned nanocrystal solid is the potential influence of spatial averaging. We first examine the role of structural chirality by analyzing the optical properties of single dipole emitters in different locations, as indicated by the A−D labels in Figure 2a.

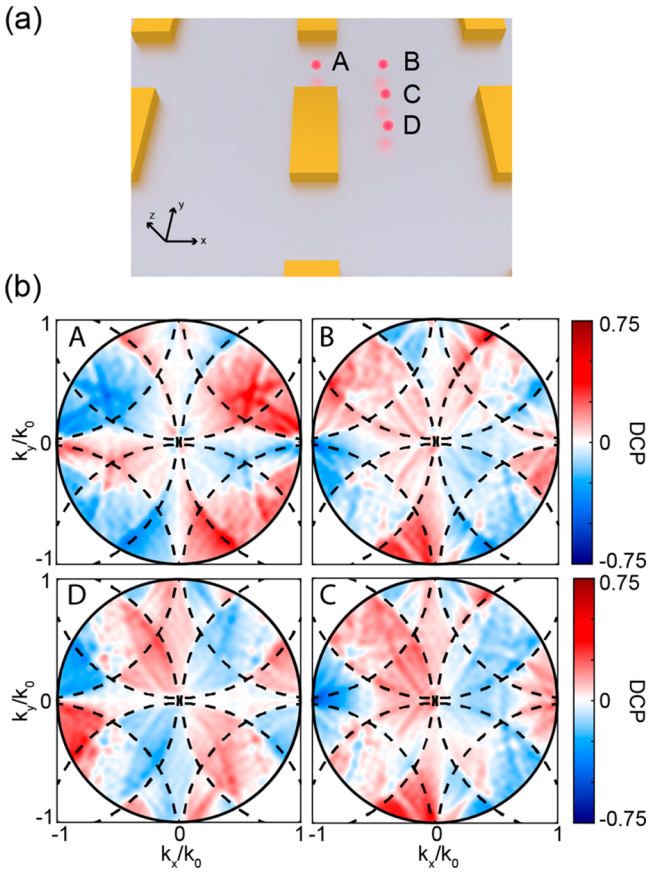

Figure 2. (a) Schematic of the gold nanobar−single dipole emitter system with positions of the emitters marked. (b) Fourier-space DCP maps of a single unpolarized light emitter placed in positions A−D.

Here for simplicity, all the dipoles are 80 nm above the ITO thin film, and positioned at (x, y) coordinates (0, 250 nm), (250 nm, 250 nm), (250 nm, 170 nm), and (250 nm, 0 nm) relative to the center of the gold nanorod, respectively. Similar results are observed at other z-positions, as discussed later. For dipoles in air, the RW modes are present at n_{eff} = 1.03 and are shown overlaid on the PL intensity data in Figure S2. Figure 2b shows that there are significant differences between the four dipole placements, indicating that the angular distribution of DCP in the far-field is influenced by the spatial position of the light emitter, and the RW modes do not explain all the observed features. When a light emitter is placed at position A (D), the array becomes symmetric along x = 0 (y = 0), and the angular distribution of the DCP is symmetric along $\frac{k_x}{k_0}$ = 0 ($\frac{k_y}{k_0}$ = 0). As a result, no net DCP is observed when integrating DCP over all the angles. When a light emitter is placed at position B or C, the symmetry of the unit cell is broken, the system becomes chiral, and the angular distribution of the DCP becomes asymmetric. This results in a positive overall DCP when integrating over all angles.

The changes in far-field DCP with dipole location can be understood by applying the Helmholtz Reciprocity Principle.[26] The reciprocity principle states that a dipole's ability to outcouple CPL is equal to a circularly polarized plane wave's ability to incouple light to that specific position. Figure 3 shows the local electric field localization from normally incident RCP and LCP plane wave illumination, and the resulting near-field DCP profile 80 nm above the ITO thin film. RCP and LCP illumination couple strongly into opposite corners of the gold nanobar, resulting in local electric field intensities greater than 10 times that of the incident wave in the plane where the dipoles are located. Combining these results generates a C2 symmetric near-field DCP profile with quadrants 1 and 3 (2 and 4) being dominated by RCP (LCP) light incoupling. This phenomenon has been exploited in other studies for bottom-up fabrication of chiral plasmonic nanostructures using circularly polarized light.[41] Importantly, near-field DCP along the x = 0 and y = 0 symmetry axes is zero, in agreement with the normal incidence ($\frac{k_x}{k_0}$= $\frac{k_y}{k_0}$ = 0) DCP in Figure 2b for positions A and D. This result is consistent with previous experimental and theoretical work investigating the local optical chirality around achiral plasmonic structures under normally incident light.[42−44] Additionally, the positive near-field DCP in the first quadrant agrees well with the RCP PL outcoupling of positions B and C at normal incidence. Figure S3 confirms the relationship between this near-field DCP and the observed far-field DCP of an emitter placed in different locations. While the use of the Helmholtz reciprocity principle provides valuable insight into the far-field DCP projections, the near-field DCP presented in Figure 3b only provides a connection between normally incident in- and outcoupling, and similar analysis would have to be repeated for every angle of interest. Figure S3 also shows the near-field DCP data for additional angles of incidence.

A second reason for the improved PL intensity/DCP of the patterned nanocrystal solid compared to the uniform film is the role of spatial averaging. To examine the role of averaging over spatial locations, we systematically increased the number of light emitters, comparing cases with 1, 9, or 25 light emitters placed 80 nm above the substrate (Figure 4 and Figure S4). In this set of simulations, the nanobars and the dipole emitters were embedded in a dielectric slab with n = 1.59, the same as the film in Figure 1a−d. This allows for a direct comparison of the role of spatial position, without the effects of the disk resonance or a changing refractive index, which are considered later.

We examine two different cases: in the first case the dipoles are positioned at the same location as the disk in Figure 1 (Figure S4a−i), and in the other case the dipoles are positioned such that part of the ensemble overlaps the Au rod (Figure 4i−l and Figure S4p). When the dipoles are placed at the same location as the disk, there are very few changes to either the PL intensity or the DCP as additional dipoles are

https://doi.org/10.1021/acsaom.2c00130
ACS Appl. Opt. Mater. 2023, 1, 491−499

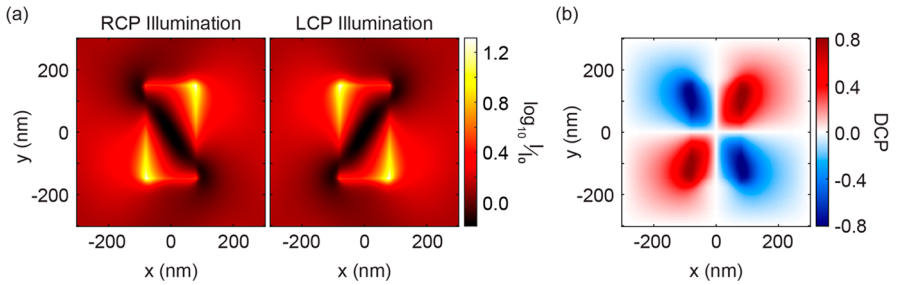

Figure 3. (a) Normal incidence RCP (left) and LCP (right) plane wave resonant field profiles 80 nm above the ITO thin film. (b) Resulting near-field DCP profile.

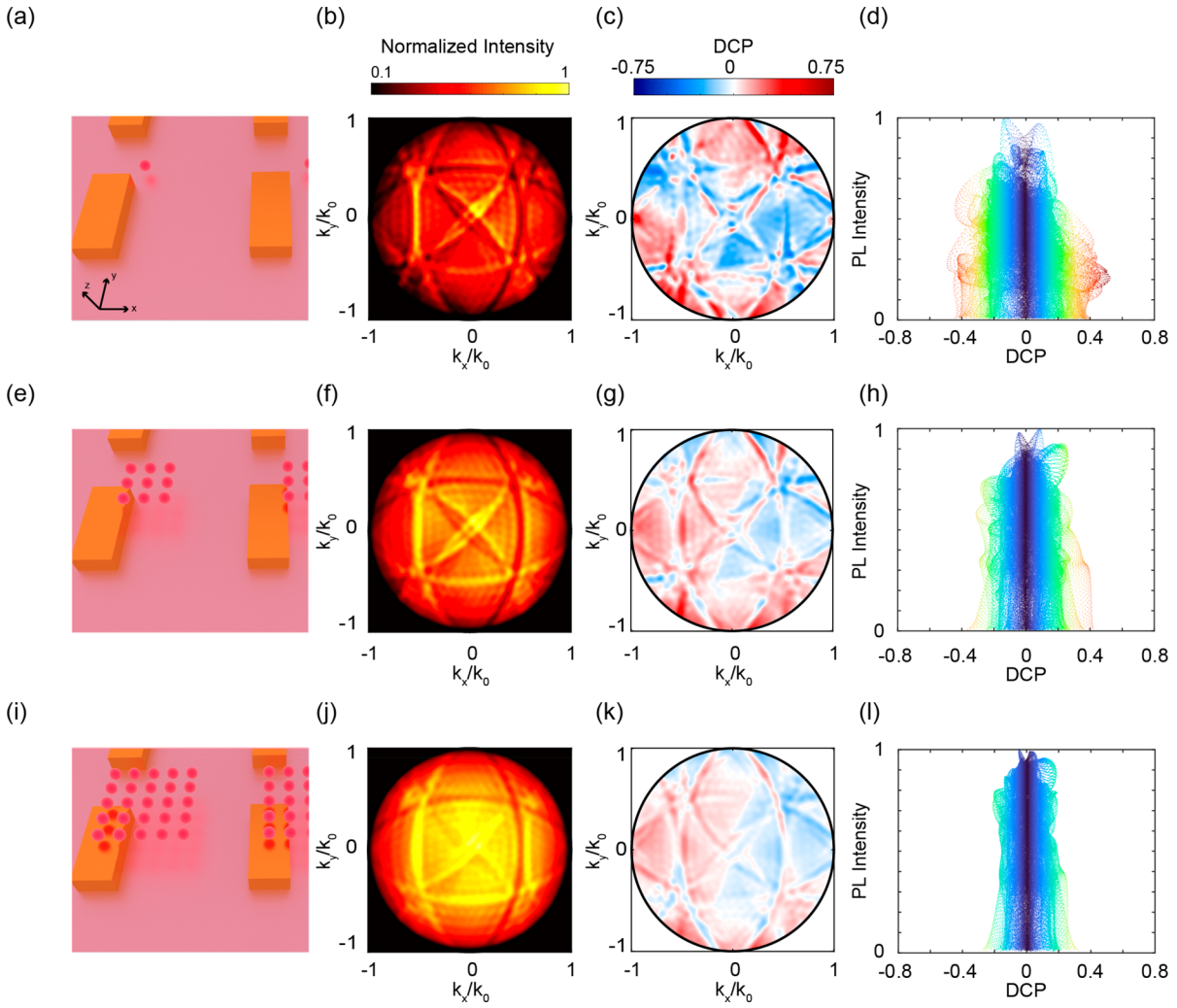

Figure 4. (a, e, i) Schematic of simulated systems with gold nanobar arrays coupled to a single dipole emitter, 9 emitters, and 25 emitters, respectively. (b, f, j) Corresponding normalized Fourier-space photoluminescence intensity calculations, (c, g, k) DCP, and (d, h, l) photoluminescence vs DCP scatter-plots where color represents the magnitude of the DCP.

added. This indicates that, with judicious placement, ensembles of dipoles can have a very similar response to systems containing individual emitters.

Figure 4i–l, however, exhibits significant differences from the single dipole case as more dipoles are added. In this case, the location of the dipoles is chosen to have partial overlap with the Au rod, where the local DCP can be significantly more complex. First, we note that the PL intensity increases and the DCP magnitude decreases as we increase the number of light emitters. For the case of the single dipole (Figure 4a–d), there are certain angles where the DCP magnitude is high, but the corresponding PL intensity at these angles is not. In the case of 9 dipoles (Figure 4e–h), the PL intensity increases along the angles that correspond to RW lines, leading to a few angles where the magnitudes of the DCP and PL are simultaneously moderately high ($|DCP| > 0.2$ and $I > 0.5$). As the number of emitters is increased to 25 (Figure 4i–l), the PL intensity is less directional, and the DCP magnitude is reduced. These results suggest that coupling an ensemble instead of a single light emitter to periodic nanostructure arrays could alter the

https://doi.org/10.1021/acsaom.2c00130
ACS Appl. Opt. Mater. 2023, 1, 491–499

polarization and directionality of PL intensity in the far-field while maintaining high DCP and that precise placement of single emitters is not necessarily required.

The real structure, of course, does not consist of dipoles at a single height embedded in a uniform refractive index polymer, but of luminescent material arranged into a pillar with a cladding medium of air. One effect of this change derives from the disk's refractive index, which slightly perturbs the resonance of the Au nanobar away from air. This can be seen by examining the scattering cross section of the Au−nanodisk system (Figure S5), which closely matches that of the Au−air system for most wavelengths between 300 and 1000 nm. This effect is also illustrated by Figure S6a, which shows that the disk slightly perturbs the near-field DCP distribution of the Au nanobar at a height of 80 nm compared to the Au-only system in Figure 3b. The second effect of the Au-nanodisk system comes from averaging over different dipole polarizations. In the data shown in Figures 1 and 4, we considered a single height of the dipole, but averaged over all the dipole orientations. Figure 5 isolates the effect of dipole orientation and shows the k-space PL intensity data for the case where all the dipole sources inside the nanopillar inject light polarized along the x, y, or z directions, respectively. Different polarizations of the injected EM radiation selectively couple to the different EM modes supported by the system, with light polarized along the x and y directions matching the calculated RW anomalies of the n_{eff} = 1.55 mode, and the z-polarized light matching the RW diffraction lines from both the n_{eff} = 1.03 and n_{eff} = 1.55 modes. As for the effect of dipole height, the magnitude and sign of the far-field DCP along specific RW lines are similar regardless of the vertical position of the light emitters inside the luminescent nanopillar, varying by 0.05 between distances of 20 and 80 nm from the substrate (Figure S7).

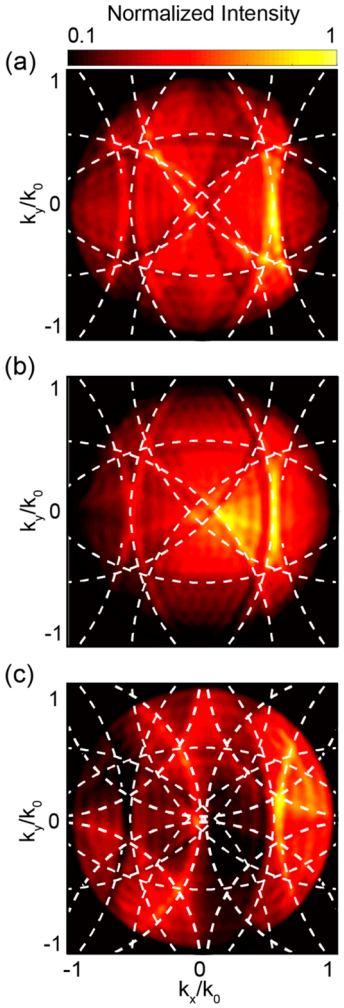

Figure 5. Angular distribution of normalized photoluminescence intensity of dipoles within the nanopillar of Figure 1e emitting light polarized along the (a) x, (b) y, and (c) z directions. The Rayleigh−Wood modes for n_{eff} = 1.55 are overlaid in all three panels, along with those for n_{eff} = 1.03 in panel c.

Finally, realistic systems are not single wavelength emitters but instead emit over a range of wavelengths. The light emitters simulated in this study are based on CdSe/CdS core/shell QDs, which have a PL emission maximum at 630 nm ±2 nm and a full width at half-maximum (fwhm) of 30 nm. We investigated the effects of the fwhm on the far-field DCP and PL intensity by simulating a system similar to Figure 1e with varying peak PL wavelength: either 615, 630, or 645 nm (Figure S8). In this case, however, the light emitters are only placed at 80 nm above the surface of ITO. We see that the k-space PL intensity data varies based on the wavelength of dipole emission, but the DCP data remains similar across different wavelengths. When we perform a weighted average of the PL and DCP data, as would be the case for a polydisperse ensemble of nanocrystals, we see that the average DCP and PL data resembles the data for 630 nm emission but is slightly less sharp, and the RW lines are slightly less apparent. This is because each wavelength supports a slightly different effective refractive index mode: PL at 615 nm matches the RW diffraction lines for the n_{eff} = 1.56 and n_{eff} = 1.06 modes, PL at 630 nm matches the RW diffraction lines for the n_{eff} = 1.55 and n_{eff} = 1.06 modes, and PL at 645 nm matches the RW diffraction lines for the n_{eff} = 1.55 and n_{eff} = 1.00 modes. The transmission spectrum of the Au NR array also changes with pitch, as shown in Figure S9. In general, increasing the pitch increases the wavelength at which a minimum in the transmission spectrum occurs. For a pitch of 600 nm, there is a minimum in the transmission spectrum at λ = 645 nm; at pitch = 580 nm, the minimum shifts to λ = 630 nm, and at pitch = 550 nm, the transmission spectrum minimum occurs at λ = 613 nm.

We now suggest a route to choose the position and shape of the light-emitting solid to maximize both PL intensity and DCP at a targeted angle of outcoupling, using the Helmholtz reciprocity principle. We first ran a series of simulations with RCP and LCP plane waves incident at different angles along the known n_{eff} = 1.03 RW mode lines. We considered angles of incidence ranging from near-normal to grazing and assigned each angle of incidence (AOI) a number from 1 to 48. Figure S10 and Table S1 give the corresponding $(\frac{k_x}{k_0}, \frac{k_y}{k_0})$ vector and (θ, φ) for each AOI. For every spatial position in the unit cell, we determined which angle of incidence had the maximum difference in near-field circularly polarized field intensity enhancement using the figure of merit $\left(\frac{I}{I_0}\right)_{RCP} - \left(\frac{I}{I_0}\right)_{LCP}$, as shown in Figure 6a. Locations where this figure of merit is maximized favor RCP in- and outcoupling at that particular angle, while locations where this figure of merit is minimized favor LCP in- and outcoupling. Figure 6b shows the corresponding calculation where dipoles are now placed in

https://doi.org/10.1021/acsaom.2c00130
ACS Appl. Opt. Mater. 2023, 1, 491−499

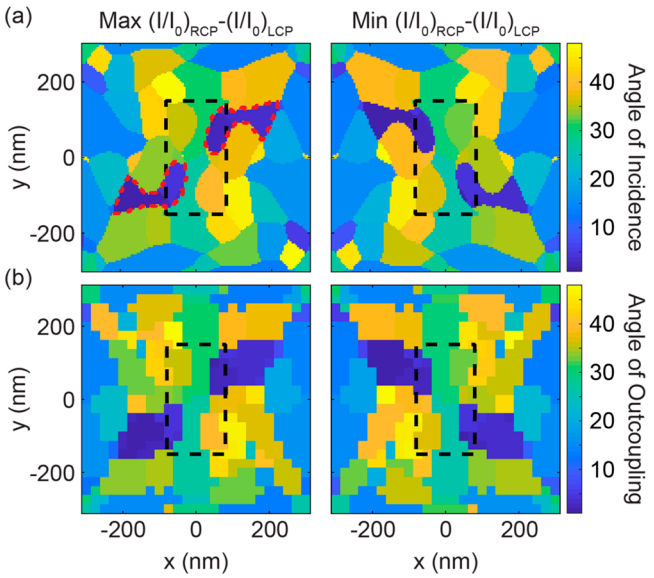

Figure 6. Spatial calculations of the angle at which the maximum difference in circularly polarized field intensity enhancement is observed as (a) the angle of incidence is varied or (b) the angle of outcoupling is observed and the dipole position is moved. The location of the Au NR is outlined in a dashed black line.

different positions across the unit cell. For each dipole position, the far-field angular distribution $\left(\frac{I}{I_0}\right)_{RCP} - \left(\frac{I}{I_0}\right)_{LCP}$ is calculated, and then the angle at which this figure of merit is either maximized or minimized is recorded at each dipole location. The two data sets in Figure 6a,b show good agreement, and it is considerably less computationally intensive to calculate the former. Both data sets exhibit C2 symmetry, matching the symmetry of the Au NR array.

The difference in circularly polarized field intensity enhancement was chosen as the figure of merit because it contains information on both the strength and polarization selectivity of light incoupling. However, different figures of merit can be utilized depending on the importance of the photoluminescence strength and polarization selectivity for the given application. Similar spatial calculations of the angle at which circularly polarized photoluminescence is maximized using other figures of merit are included in Figure S11. Using circularly polarized field intensity enhancement $\left(\frac{I}{I_0}\right)_{RCP/LCP}$ as the figure of merit maximizes the importance of circularly polarized photoluminescence intensity but does not contain polarization selectivity information as only one polarization is considered at a time. Conversely, using DCP $\left(\frac{I_{RCP} - I_{LCP}}{I_{RCP} + I_{LCP}}\right)$ as the figure of merit maximizes the importance of circular polarization selectivity, but does not contain PL intensity information.

We can now design a system that outcouples an arbitrary circular polarization of light at an arbitrary angle. If we chose, for example, to make a structure that preferentially outcouples RCP light at the normal direction, then we would place dipoles around the two regions that preferentially incouple normally incident RCP light, as outlined with the dotted lines in Figure 6a. The resulting PL intensity and DCP in the far-field obtained by placing dipoles in those locations is shown in Figure 7. The designed light-emitting metamaterial shows large PL intensity at normal incidence ($\frac{k_x}{k_0} = \frac{k_y}{k_0} = 0$) that is strongly right-handed circularly polarized. Figure 7d combines the PL intensity and DCP data, indicating that this system exhibits highly directional, polarized PL.

Finally, we note a few differences when the underlying Au pattern changes to a chiral pattern. This array consists of two Au nanobars offset by 150 nm and spaced apart from one another by a gap of 80 nm. The Au nanobars have the same dimensions and periodicity as those used within the single nanobar array. Figure S12 shows the equivalent calculation to Figure 6 and illustrates the spatial locations where different angles of incidence yield maximum difference in circularly polarized electric field intensity enhancement. Unlike the single nanobar case, the locations for RCP-emitting devices and LCP-emitting devices are no longer symmetric. If these structures were coated by a uniform film of light emitters, the PL integrated over the outcoupled angles would exhibit left-handed circular polarization.[15,39]

However, here we show that judicious placement of the dipoles generates circularly polarized light-emitting metasurfaces of either polarization, regardless of the underlying pattern, as shown in Figure 8. The dipole locations of the light-emitting metasurfaces were selected to maximize the outcoupling of either RCP (Figure 8a) or LCP (Figure 8e) PL at $\theta = 15.8°$, $\phi = 78.3°$ and $\theta = 15.8°$, $\phi = 258.3°$, where θ and ϕ are given by a spherical coordinate system where θ is the polar angle and ϕ is the azimuthal angle. These off-normal angles were arbitrarily

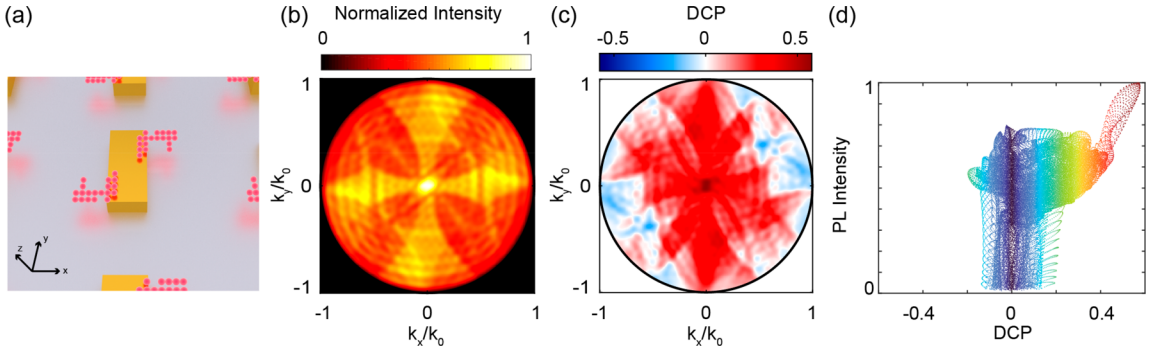

Figure 7. (a) Schematic of the simulated system consisting of a gold nanobar array and strategically placed dipole emitters to generate a normal incidence RCP light-emitting metamaterial. Corresponding (b) normalized Fourier-space photoluminescence intensity calculations, (c) DCP, and (d) photoluminescence vs DCP scatterplot where color represents the magnitude of DCP.

https://doi.org/10.1021/acsaom.2c00130
ACS Appl. Opt. Mater. 2023, 1, 491−499

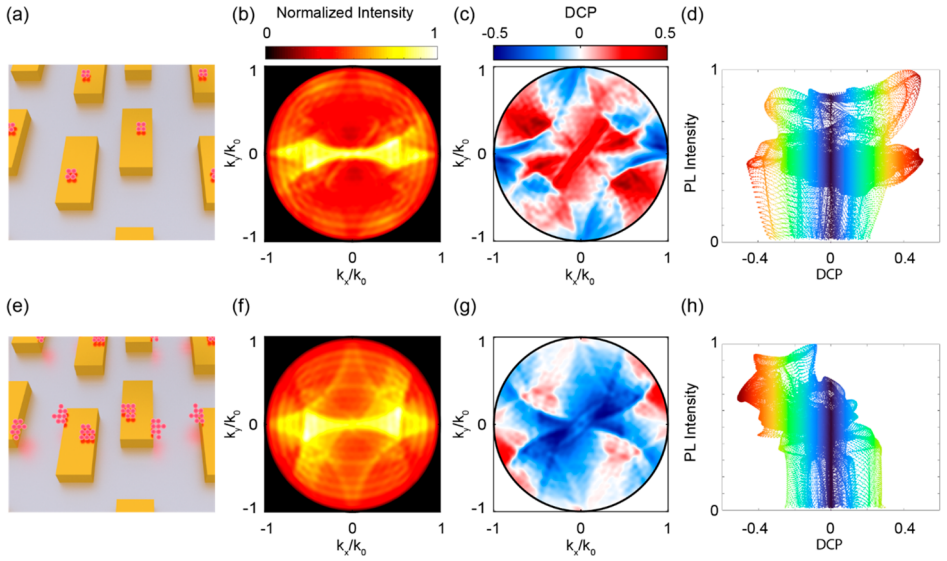

Figure 8. (a) Schematic of the simulated system consisting of an offset gold nanobar array and strategically placed dipole emitters to generate an RCP light-emitting metasurface at $\frac{k_x}{k_0}$ = 0.27, $\frac{k_y}{k_0}$ = 0.06 and $\frac{k_x}{k_0}$ = −0.27, $\frac{k_y}{k_0}$ = −0.06. Corresponding (b) normalized Fourier-space photoluminescence intensity calculations, (c) DCP, and (d) photoluminescence vs DCP scatter-plot where color represents the magnitude of DCP. (e−h) LCP light emitting.

selected and are given by $\frac{k_x}{k_0}$ = 0.27, $\frac{k_y}{k_0}$ = 0.06 and $\frac{k_x}{k_0}$ = −0.27, $\frac{k_y}{k_0}$ = −0.06 (AOI 5 and AOI 9 in Table S1). Figure 8b,f shows that the PL intensity is very similar between these two cases, but the DCP data (Figure 8c,g) indicates that opposite polarization light is emitted at many angles (and when integrating over all the angles). Figure 8d,h compares these results, showing that, as in the case of the single nanobar above, these structures emit polarized light with simultaneously high intensity.

CONCLUSIONS

In summary, we showed that the deliberate placement of a luminescent nanostructure in the unit cell of a metasurface creates systems with a higher magnitude of DCP than systems where the metasurface is covered uniformly by a luminescent film and that the areas of high DCP are efficiently out-coupled to the far-field. Simulations of gold nanobar arrays coupled to different numbers of light emitters showed that the different and sometimes competing dissymmetry of RCP and LCP PL intensity of individual light emitters can alter the magnitude and potentially the sign of DCP as more light emitters are added to the ensemble. Guided by these studies, we developed a method for determining the optimal position and shape of a light-emitting solid to simultaneously achieve high PL intensity and DCP at any chosen angle of emission from a general hybrid plasmonic/luminescent metamaterial system. We have shown that this method can be used for simple plasmonic metamaterial geometries such as a single nanobar but can also be extended to complex chiral geometries like offset nanobars. The simulation results are applicable to any ensemble of incoherent, unpolarized dipole emitters such as molecular dyes, and are not limited to quantum dots. Our method relies on information about near-field chiral enhancements, which is less computationally expensive than far-field calculations. Additionally, rather than being a "guess and check" method, our method enables the rational design of light-emitting metamaterials to satisfy an arbitrary directionality of PL and sign of DCP. These systems can be realized experimentally with fabrication techniques such as direct-write electron-beam lithography. The resulting highly tailored optical devices can be used for a variety of applications where polarization and directional control of PL can be achieved with metamaterials, including solid-state lighting, beaming, and display technologies.[26,45] Additionally, devices based on the metamaterial systems presented here could be used for enhanced sensing and imaging of microscopic objects.[46,47]

METHOD OF CALCULATION

The numerical electromagnetic calculations were performed using Lumerical Solutions. The light emitters are electric dipoles that emit at λ_{PL} = 630 nm and have a full width at half-maximum (fwhm) of 140 nm, as shown in Figure S13. For every spatial position of dipole considered, three separate simulations were performed with the dipole oriented along the *x*, *y*, or *z* direction. The resulting intensity of the electromagnetic fields in the far-field can be added together incoherently to capture the response of an incoherent, unpolarized dipole. For each of the cases of ensemble emitters (when not otherwise specified), we ran a sufficient number of simulations with single dipole emitters placed in an array of 23 × 23 unit cells to ensure that the results did not significantly change. Perfectly Matched Layer boundary conditions were used in all directions. The complex refractive index data for Au and for the light-emitting structures was taken from our own experimental measurements, based on spectroscopic ellipsometry measurements of nanocrystal solids.[33]

ASSOCIATED CONTENT

Supporting Information

The Supporting Information is available free of charge at https://pubs.acs.org/doi/10.1021/acsaom.2c00130.

Calculation of the Rayleigh−Wood modes, additional PL intensity data from the single dipoles, comparison of

https://doi.org/10.1021/acsaom.2c00130
ACS Appl. Opt. Mater. 2023, 1, 491−499

the near- and far-field DCP calculations, calculations of the PL intensity and DCP as the number of dipoles increases at alternate locations, scattering cross sections of the nanostructures, Fourier-space PL and DCP calculations as a function of height of the emitter, additional near-field DCP analysis, analysis of the spectral dependence of emitters on Fourier-space PL and DCP, additional details of the design procedure for choosing dipole locations for both the single nanobars and pairs of nanobars, the intensity profile of a dipole source, and data reproduced from Pachidis et al.[39] using our simulation method (PDF)

AUTHOR INFORMATION

Corresponding Author

Vivian E. Ferry − *Department of Chemical Engineering and Materials Science, University of Minnesota, Minneapolis, Minnesota 55455, United States;* orcid.org/0000-0002-9676-6056; Email: veferry@umn.edu

Authors

Maya Ramamurthy − *Department of Chemical Engineering and Materials Science, University of Minnesota, Minneapolis, Minnesota 55455, United States;* orcid.org/0000-0003-2882-9024

Pavlos Pachidis − *Department of Chemical Engineering and Materials Science, University of Minnesota, Minneapolis, Minnesota 55455, United States*

Bryan M. Cote − *Department of Chemical Engineering and Materials Science, University of Minnesota, Minneapolis, Minnesota 55455, United States*

Complete contact information is available at: https://pubs.acs.org/10.1021/acsaom.2c00130

Notes

The authors declare no competing financial interest.

ACKNOWLEDGMENTS

A portion of this work was supported by the Marion Milligan Mason Award for Women in the Chemical Sciences. A portion of this work was supported by the National Science Foundation under Award 2102835. M.R. was supported by an NSF graduate fellowship. The authors acknowledge the Minnesota Supercomputing Institute (MSI) at the University of Minnesota for providing resources that contributed to the research results reported within this paper.

REFERENCES

(1) Yu, N.; Genevet, P.; Kats, M. A.; Aieta, F.; Tetienne, J. P.; Capasso, F.; Gaburro, Z. Light Propagation with Phase Discontinuities: Generalized Laws of Reflection and Refraction. *Science* **2011**, *334* (6054), 333.

(2) Poulikakos, L. V.; Thureja, P.; Stollmann, A.; De Leo, E.; Norris, D. J. Chiral Light Design and Detection Inspired by Optical Antenna Theory. *Nano Lett.* **2018**, *18* (8), 4633.

(3) Plum, E. Extrinsic Chirality: Tunable Optically Active Reflectors and Perfect Absorbers. *Appl. Phys. Lett.* **2016**, *108* (24), 241905.

(4) De Leon, I.; Horton, M. J.; Schulz, S. A.; Upham, J.; Banzer, P.; Boyd, R. W. Strong, Spectrally-Tunable Chirality in Diffractive Metasurfaces. *Sci. Rep.* **2015**, *5*, 13034.

(5) Ferry, V. E.; Hentschel, M.; Alivisatos, A. P. Circular Dichroism in Off-Resonantly Coupled Plasmonic Nanosystems. *Nano Lett.* **2015**, *15* (12), 8336.

(6) Neubrech, F.; Hentschel, M.; Liu, N. Reconfigurable Plasmonic Chirality: Fundamentals and Applications. *Adv. Mater.* **2020**, *32* (41), 1905640.

(7) Solomon, M. L.; Hu, J.; Lawrence, M.; García-Etxarri, A.; Dionne, J. A. Enantiospecific Optical Enhancement of Chiral Sensing and Separation with Dielectric Metasurfaces. *ACS Photonics* **2019**, *6* (1), 43−49.

(8) Jun, Y. C.; Huang, K. C. Y.; Brongersma, M. L. Plasmonic Beaming and Active Control over Fluorescent Emission. *Nat. Commun.* **2011**, *2* (1), 283.

(9) Kildishev, A. V.; Boltasseva, A.; Shalaev, V. M. Planar Photonics with Metasurfaces. *Science.* **2013**, *339*, 1232009.

(10) Prins, F.; Kim, D. K.; Cui, J.; De Leo, E.; Spiegel, L. L.; McPeak, K. M.; Norris, D. J. Direct Patterning of Colloidal Quantum-Dot Thin Films for Enhanced and Spectrally Selective Out-Coupling of Emission. *Nano Lett.* **2017**, *17* (3), 1319.

(11) Wu, Q.; Liu, B.; Zhu, Z.; Gu, M.; Chen, H.; Xue, C.; Zhao, J.; Wu, Y.; Tai, R.; Ouyang, X. Directional Emission of Plastic Luminescent Films Using Photonic Crystals Fabricated by Soft-X-Ray Interference Lithography and Reactive Ion Etching. *Sci. Rep.* **2018**, *8* (1), 9254.

(12) Kravets, V. G.; Kabashin, A. V.; Barnes, W. L.; Grigorenko, A. N. Plasmonic Surface Lattice Resonances: A Review of Properties and Applications. *Chem. Rev.* **2018**, *118*, 5912.

(13) De Leo, E.; Cocina, A.; Tiwari, P.; Poulikakos, L. V.; Marqués-Gallego, P.; Le Feber, B.; Norris, D. J.; Prins, F. Polarization Multiplexing of Fluorescent Emission Using Multiresonant Plasmonic Antennas. *ACS Nano* **2017**, *11* (12), 12167.

(14) Meinzer, N.; Hendry, E.; Barnes, W. L. Probing the Chiral Nature of Electromagnetic Fields Surrounding Plasmonic Nanostructures. *Phys. Rev. B - Condens. Matter Mater. Phys.* **2013**, *88* (4), 1−5.

(15) Cotrufo, M.; Osorio, C. I.; Koenderink, A. F. Spin-Dependent Emission from Arrays of Planar Chiral Nanoantennas Due to Lattice and Localized Plasmon Resonances. *ACS Nano* **2016**, *10* (3), 3389−3397.

(16) Baev, A.; Prasad, P. N.; Ågren, H.; Samoć, M.; Wegener, M. Metaphotonics: An Emerging Field with Opportunities and Challenges. *Physics Reports.* **2015**, *594*, 1.

(17) Lodahl, P.; Mahmoodian, S.; Stobbe, S.; Rauschenbeutel, A.; Schneeweiss, P.; Volz, J.; Pichler, H.; Zoller, P. Chiral Quantum Optics. *Nature* **2017**, *541* (7638), 473−480.

(18) Zheludev, N. I. The Road Ahead for Metamaterials. *Science (80-.).* **2010**, *328* (5978), 582−583.

(19) Yan, C.; Wang, X.; Raziman, T. V.; Martin, O. J. F. Twisting Fluorescence through Extrinsic Chiral Antennas. *Nano Lett.* **2017**, *17* (4), 2265−2272.

(20) Kruk, S. S.; Decker, M.; Staude, I.; Schlecht, S.; Greppmair, M.; Neshev, D. N.; Kivshar, Y. S. Spin-Polarized Photon Emission by Resonant Multipolar Nanoantennas. *ACS Photonics* **2014**, *1* (11), 1218−1223.

(21) Wang, Z.; Wang, Y.; Adamo, G.; Teng, J.; Sun, H. Induced Optical Chirality and Circularly Polarized Emission from Achiral CdSe/ZnS Quantum Dots via Resonantly Coupling with Plasmonic Chiral Metasurfaces. *Laser Photonics Rev.* **2019**, *13* (3), 1800276.

(22) Liu, S.; Vaskin, A.; Addamane, S.; Leung, B.; Tsai, M. C.; Yang, Y.; Vabishchevich, P. P.; Keeler, G. A.; Wang, G.; He, X. Light-Emitting Metasurfaces: Simultaneous Control of Spontaneous Emission and Far-Field Radiation. *Nano Lett.* **2018**, *18* (11), 6906.

(23) Le, K. Q.; Hashiyada, S.; Kondo, M.; Okamoto, H. Circularly Polarized Photoluminescence from Achiral Dye Molecules Induced by Plasmonic Two-Dimensional Chiral Nanostructures. *J. Phys. Chem. C* **2018**, *122* (43), 24924−24932.

(24) Giannini, V.; Fernández-Domínguez, A. I.; Heck, S. C.; Maier, S. A. Plasmonic Nanoantennas: Fundamentals and Their Use in Controlling the Radiative Properties of Nanoemitters. *Chem. Rev.* **2011**, *111* (6), 3888−3912.

(25) Curto, A. G.; Volpe, G.; Taminiau, T. H.; Kreuzer, M. P.; Quidant, R.; Van Hulst, N. F. Unidirectional Emission of a Quantum

Dot Coupled to a Nanoantenna. *Science (80-.).* **2010**, *329* (5994), 930.
(26) Vaskin, A.; Kolkowski, R.; Koenderink, A. F.; Staude, I. *Light-Emitting Metasurfaces.* **2019**, *8* (7), 1151−1198.
(27) Nandwana, V.; Subramani, C.; Yeh, Y. C.; Yang, B.; Dickert, S.; Barnes, M. D.; Tuominen, M. T.; Rotello, V. M. Direct Patterning of Quantum Dot Nanostructures via Electron Beam Lithography. *J. Mater. Chem.* **2011**, *21* (42), 16859−16862.
(28) Miszta, K.; Greullet, F.; Marras, S.; Prato, M.; Toma, A.; Arciniegas, M.; Manna, L.; Krahne, R. Nanocrystal Film Patterning by Inhibiting Cation Exchange via Electron-Beam or X-Ray Lithography. *Nano Lett.* **2014**, *14* (4), 2116−2122.
(29) Palazon, F.; Prato, M.; Manna, L. Writing on Nanocrystals: Patterning Colloidal Inorganic Nanocrystal Films through Irradiation-Induced Chemical Transformations of Surface Ligands. *J. Am. Chem. Soc.* **2017**, *139* (38), 13250−13259.
(30) Wang, Y.; Pan, J. A.; Wu, H.; Talapin, D. V. Direct Wavelength-Selective Optical and Electron-Beam Lithography of Functional Inorganic Nanomaterials. *ACS Nano* **2019**, *13* (12), 13917−13931.
(31) Dement, D. B.; Quan, M. K.; Ferry, V. E. Nanoscale Patterning of Colloidal Nanocrystal Films for Nanophotonic Applications Using Direct Write Electron Beam Lithography. *ACS Appl. Mater. Interfaces* **2019**, *11* (16), 14970−14979.
(32) Maoz, B. M.; Ben Moshe, A.; Vestler, D.; Bar-Elli, O.; Markovich, G. Chiroptical Effects in Planar Achiral Plasmonic Oriented Nanohole Arrays. *Nano Lett.* **2012**, *12* (5), 2357.
(33) Dement, D. B.; Puri, M.; Ferry, V. E. Determining the Complex Refractive Index of Neat CdSe/CdS Quantum Dot Films. *J. Phys. Chem. C* **2018**, *122* (37), 21557−21568.
(34) Sersic, I.; Tuambilangana, C.; Koenderink, A. F. Fourier Microscopy of Single Plasmonic Scatterers. *New J. Phys.* **2011**, *13*, 083019.
(35) Dominguez, D.; Alharbi, N.; Alhusain, M.; Bernussi, A. A.; Peralta, L. G. De. Fourier Plane Imaging Microscopy. *J. Appl. Phys.* **2014**, *116* (10), 103102.
(36) Bryche, J. F.; Barbillon, G.; Bartenlian, B.; Dujardin, G.; Boer-Duchemin, E.; Le Moal, E. K -Space Optical Microscopy of Nanoparticle Arrays: Opportunities and Artifacts. *J. Appl. Phys.* **2018**, *124* (4), 043102.
(37) Röhrich, R.; Hoekmeijer, C.; Osorio, C. I.; Koenderink, A. F. Quantifying Single Plasmonic Nanostructure Far-Fields with Interferometric and Polarimetric k-Space Microscopy. *Light Sci. Appl.* **2018**, *7* (1), 65.
(38) Rigneault, H.; Lemarchand, F.; Sentenac, A. Dipole Radiation into Grating Structures. *J. Opt. Soc. Am. A* **2000**, *17* (6), 1048.
(39) Pachidis, P.; Cote, B. M.; Ferry, V. E. Tuning the Polarization and Directionality of Photoluminescence of Achiral Quantum Dot Films with Chiral Nanorod Dimer Arrays: Implications for Luminescent Applications. *ACS Appl. Nano Mater.* **2019**, *2* (9), 5681−5687.
(40) Lozano, G.; Grzela, G.; Verschuuren, M. A.; Ramezani, M.; Rivas, J. G. Tailor-Made Directional Emission in Nanoimprinted Plasmonic-Based Light-Emitting Devices. *Nanoscale* **2014**, *6* (15), 9223.
(41) Saito, K.; Tatsuma, T. Chiral Plasmonic Nanostructures Fabricated by Circularly Polarized Light. *Nano Lett.* **2018**, *18* (5), 3209.
(42) Schäferling, M.; Yin, X.; Giessen, H. Formation of Chiral Fields in a Symmetric Environment. *Opt. Express* **2012**, *20* (24), 26326.
(43) Schäferling, M.*Chiral Nanophotonics: Chiral Optical Properties of Plasmonic Systems*; Springer Nature, 2017.
(44) Hashiyada, S.; Narushima, T.; Okamoto, H. Imaging Chirality of Optical Fields near Achiral Metal Nanostructures Excited with Linearly Polarized Light. *ACS Photonics* **2018**, *5* (4), 1486.
(45) Munkhbat, B.; Pöhl, H.; Denk, P.; Klar, T. A.; Scharber, M. C.; Hrelescu, C. Performance Boost of Organic Light-Emitting Diodes with Plasmonic Nanostars. *Adv. Opt. Mater.* **2016**, *4* (5), 772.
(46) Bontempi, N.; Chong, K. E.; Orton, H. W.; Staude, I.; Choi, D. Y.; Alessandri, I.; Kivshar, Y. S.; Neshev, D. N. Highly Sensitive Biosensors Based on All-Dielectric Nanoresonators. *Nanoscale* **2017**, *9* (15), 4972.
(47) Tittl, A.; Leitis, A.; Liu, M.; Yesilkoy, F.; Choi, D. Y.; Neshev, D. N.; Kivshar, Y. S.; Altug, H. Imaging-Based Molecular Barcoding with Pixelated Dielectric Metasurfaces. *Science (80-.).* **2018**, *360* (6393), 1105.

https://doi.org/10.1021/acsaom.2c00130
ACS Appl. Opt. Mater. 2023, 1, 491−499